Supplementary information to "Massive sediment pulses triggered by a multi-stage alpine cliff fall (Hochvogel, DE/AT)"

Natalie Barbosa[1,2], Johannes Leinauer[2], Juilson Jubanski[3], Michael Dietze[4,5], Ulrich Münzer[6], Florian Siegert[1,3], Michael Krautblatter[2].

[1]Department of Earth and Environmental Sciences, Faculty of Earth Sciences, GeoBio Center, Ludwig-Maximilians-University, Munich, 80333, Germany.
[2]Chair of Landslide Research, Technical University of Munich, Munich, 80333, Germany
[3]3D RealityMaps GmbH, Munich, 81673, Germany
[4]Faculty of Geosciences and Geography, Georg-August-Universität Göttingen, Göttingen, 31073, Germany
[5]GFZ German Research Centre for Geosciences, Potsdam, 14473, Germany
[6]Department of Earth and Environmental Sciences, Section Geology, Ludwig-Maximilians-University, Munich, 80333, Germany.

Correspondence to: Natalie Barbosa (barbosa@biologie.uni-muenchen.de)

1. Multi-temporal quantification of surface change

1.1. Datasets

We used large format aerial imagery surveyed by the Bundesamt für Eich- und Vermessungswesen (BEV); the Landesamt für Digitalisierung, Breitband und Vermessung (LDBV); and the company 3D RealityMaps. Detail information on the aerial surveys is listed in Table 1.

Table 1. Detail information on the aerial surveys. Bundesamt für Eich- und Vermessungswesen (BEV). Landesamt für Digitalisierung, Breitband und Vermessung (LDBV)

Year	Source	Date	Coverage (km2)	Image overlap	Resolution	Camera (focal lenght mm)
2009	LDBV	29.07.2009	36 km2	80:50	20 cm	UltraCam- X (100.5)
2010	BEV	12.09.2010	48	80:60	20 cm	UltraCam-Xp (100.5)
2012	LDBV	20.08.2012	45 km2	80:50	20 cm	UltraCam- XP (100.5)
2014	BEV	23.09.2014	48	80:60	20 cm	UltraCam-Eagle M1 (100.5)
2015	LDBV	30.06.2015, 01.07.2015	55 km2	80:50	20 cm	UltraCam XP (100.5)
2017	BEV	07.08.2017	125.10	80:60	20 cm	UltraCam-Eagle M1 (100.5)
2018	**3DRM**	**20.9.2018 21.9.2018**	**48 km2**	**80:70**	**10 cm**	**UltraCam-Eagle M2** (100.5)
2020	LDBV	27.07.2020, 28.07.2020, 21.08.2020, 04.09.2020	55.77	80:50	20 cm	UltraCam-Eagle M3 (100.5)

1.2. 3D-coregistration evaluation

The 3D-coregistration successfully align the datasets within a spatial uncertainty close to the spatial resolution. Table 2 summarizes the metrics used to later estimate the critical thresholds for change detection.

Table 2. Assessment of the 3D-coregistration for each dataset.

Time periods of change	N points	RMSE	RMSE X	RMSE Y	RMSE Z
2010	25	0.203	0.074	0.086	0.168
2012	19	0.203	0.078	0.102	0.157
2014	13	0.211	0.118	0.132	0.113
2015	17	0.197	0.072	0.086	0.162
2017	30	0.191	0.103	0.091	0.133
2018			Reference		
2020	27	0.136	0.064	0.047	0.11

Additionally, we independently evaluate the elevation uncertainty after the 3D-coregistration using additional 30 independent well-distributed points on stable areas with a complex topography and close to the area of interest. The location of the points is presented in Figure 1. The elevation uncertainty, measured as the RMSE of the elevation difference in stable areas with complex topography, ranges from 30 to 40 cm depending on the combination of datasets. The combination used for this publication is summarized in Table 3.

Table 3. Elevation uncertainty

Time periods of change	Z_RMSE
2010-2012	0.343
2012-2014	0.335
2014-2015	0.296
2015-2017	0.375
2017-2018	0.382
2018-2020	0.297

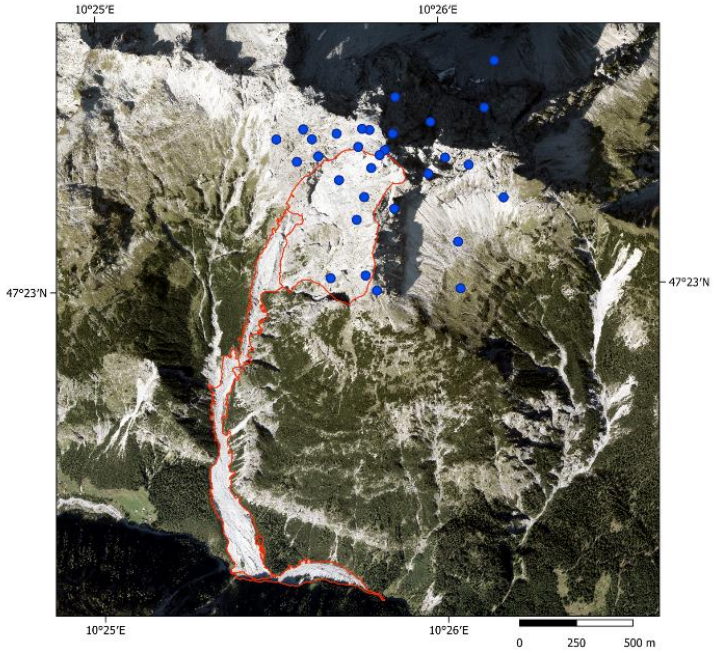

Figure 1. Distribution of points to assess the elevation uncertainty after the 3D-coregistration. We decided to focus on the upper slope because is the area with the highest theoretical uncertainty due to topography complexity.

The proposed 3D-coregistration workflow resulted in consistent landscape representations through time evidenced by topographic profiles extracted from the DSM. Profiles at strategic locations support the interpretation of the sediment cascades (Figure 2).

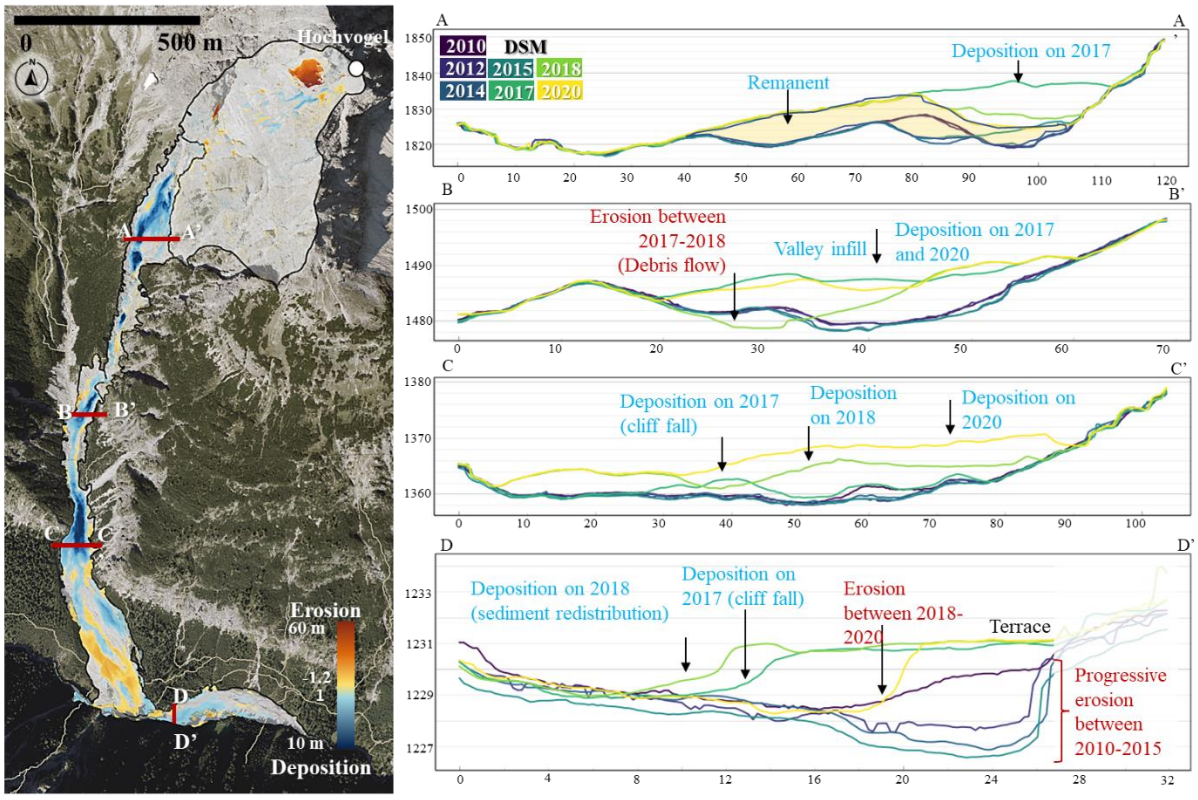

Figure 2. Topographic profiles at retention basins. Left: Cumulative topographic changes between 2010 and 2020. Dark blue areas indicate remaining sediment deposits with more than 10m in elevation. Profile A-A' shows the formation of a depositional geoform (sediment talus) which is partially eroded in the next few years. Blue polygon highlights the

remanent sediment wedge with a depth of c.a. 10 m. Profile B-B' is located in the transfer zone between the Weittal valley and the lower valley. The confined valley is filled with sediment transferred from the cliff fall in 2017, partially eroded between 2017-2018, and filled again with sediment produced by secondary rockfalls and debris flows in 2020. Profile C-C' exhibits the dynamic of the confined fan apex which is slightly affected by the primary sediment produced during the cliff event but heavily impacted by the cascades. Progressive aggradation since 2017 evidenced the sediment waves in the system. Profile D-D', shows the formation and current erosion of a terrace formed as a result of the sediment that reached the outlet of the Wildenbach catchment. An initial sediment wave blocked partially the Jochbach river by c.a. 3 m of sediment. Additional sediment was annexed to the terrace in 2018. Currently, a remnant of 3 m. width is observed, less than half of the original terrace.

1.3. Critical thresholds

1.3.1. Frequency-magnitude curves

The polygons interpreted as primary and secondary rockfalls used for the construction of the decadal frequency-magnitude curves are based on the segmentation according to the critical thresholds determined by best practice and summarized in Table 4.

Table 4. Critical threshold for the four slopes that constitute the Hochvogel summit.

	northern slope	**western slope**	**southwestern slope**	**southeastern slope**
Erosion	1	1	1	1
Deposition	0.33	0.5	0.6	0.6

1.3.2. Cascading geomorphic sediment budgets

A sediment budget describes the input, transport, storage, and export of sediment in a geomorphic system. This concept provides an effective basis for representing the key components of the sediment delivery system within a catchment and for assembling the necessary data to elucidate, understand and predict catchment sediment delivery (Walling and Collins, 2008) and estimate related natural hazards. The geomorphic sediment budget (Wheaton et al., 2010a) is calculated as the sum of the masked DoD values of erosion (negative change) and deposition (positive change).

$$Q_{b_{in}} - Q_{b_{out}} = \frac{\Delta V_{DoD}}{\Delta t} \quad (1)$$

$$\Delta V_{DoD} = \sum V_{deposition} - \sum V_{erosion} \quad (2)$$

where $Q_{b_{in}}$ is the sediment produced, $Q_{b_{out}}$ is the sediment eroded, and ΔV_{DoD} the change in storage in a given timestamp calculated by Eq. (2). If ΔV_{DoD} is positive, there is aggradation. If the ΔV_{DoD} is negative, there is degradation.

For each region and time interval, a critical threshold for erosion and deposition was determined by best practice and summarized in Table 5.

Table 5. Critical threshold for each region and time interval.

Time interval	rockface		upper channelized debris flow channel		widened disperse debris flow channel		outlet	
	Erosion	Deposition	Erosion	Deposition	Erosion	Deposition	Erosion	Deposition
2010-2012	-1	0.33	-0.6	0.34	-0.6	0.4	-0.22	0.22
2012-2014	-0.8	0.34	-0.6	0.33	-0.4	0.4	-0.2	0.2
2014-2015	-0.4	0.8	-0.8	0.8	-0.45	0.3	-0.4	0.2
2015-2017	-1	0.6	-1	0.6	-0.4	0.5	-0.2	0.2
2017-2018	-1.2	0.4	-0.8	0.4	-0.4	0.4	-0.2	0.2
2018-2020	-0.3	0.6	-0.3	0.6	-0.3	0.6	-0.2	0.2

1.4. 2016 cliff fall event

The volume inside a manually delimited extent of the cliff fall resulted in a mean of 142,175 m^3 and a standard deviation of 3 458 m. The volume calculated for all possible combinations of time intervals is summarized in Table 6.

Table 6. 2.5. volume calculation of the cliff fall occurred in 2016 for each possible time-stamp combination. The calculation has been done based on a polygon delimitation.

2017 combinations	**Volume (m^3)**	**2018 combinations**	**Volume (m^3)**	**2020 combinations**	**Volume (m^3)**
2017-2009	*-139,326*	2018-2009	*-136,328*	2020-2009	*-140,535*
2017-2010	**-147,471**	2018-2010	**-144,201**	2020-2010	**-148,759**
2017-2012	-140,738	2018-2012	-137,940	2020-2012	-141,992
2017-2014	-141,892	2018-2014	-138,697	2020-2014	-143,123
2017-2015	-144,085	2018-2015	-140,842	2020-2015	-145,364

2. Multi-stage detachment analysis

We estimate the seismic volumes following the methodology described in Le Roy et al., 2019. They determined a relation between seismic energy E_s caused by a rock fall and its initial potential energy E_p expressed by Eq. 3:

$$E_s = aE_p{}^b \quad (3)$$

with $a = 10^{-8}$ and $b = 1.55$

With this relation, the source volume can be calculated by Eq. 4:

$$V = \frac{E_s^{\frac{1}{b}}}{agpH} \quad (4)$$

where g is the gravity constant (9.81 m s^{-2}), p is the density of the rock fall material and H is the fall height of the fallen block.

We calculated the seismic Energy Es following the equations 5,6 and 7, in Le Roy et al., 2019:

$$E_s = 2\pi rphc \int_{t_0}^{t_1} u_{env}(t)^2 e^{\alpha r} \varepsilon dt \quad (5)$$

$$u_{env}(t) = \sqrt{u(t)^2 + H(u(t)^2)} \quad (6)$$

$$u(t) = \sqrt{u^2{}_E(t) + u^2{}_N(t) + u^2{}_Z(t)} \quad (7)$$

with r being the distance between seismic station and rock fall impact, h being the thickness of the layer through which the surface waves traveled, c being the velocity of the seismic waves, t0 and t1 being the start and end times of the impact signal, $u_{env}(t)$ being the envelope of the ground velocity u(t) determined via the Hilbert transform H, α being an attenuation factor accounting for the inelastic attenuation of the waves and ε being a site effect coefficient.

2.1. Seismic stations

We used 7 seismic broadband stations from the Austrian and Bavarian earthquake observatories listed in Table 7.

***Table 7. Seismic stations. Abbreviation of sensor type according to eseis package* (Dietze, 2018a).**

ID	name	x	y	z	sensor_type	network
OBER	Oberstdorf	597 551	5 251 204	896	LE3D5S	BW[1]
PART	Partenkirchen	659 143	5 262 560	760	LE3D5S	BW[1]
ZUGS	Zugspitze	649 280	5 253 292	2650	L4C	BW[1]
DAVA	Damuels	566 566	5 237 400	1602	STS2	OE[2]
MOTA	Moosalm	658 900	5 245 627	1575	STS2	OE[2]
RETA	Reutte	632 755	5 260 801	965	STS2	OE[2]
A037A	Verwall	595 994	5 213 757	2020	TC120s	Z3[3]

[1] Department of Earth and Environmental Sciences, Geophysical Observatory, University of Munchen. (2001) via http://erde.geophysik.uni-muenchen.de/fdsnws/station/1/query?

[2] ZAMG - Zentralanstalt für Meterologie und Geodynamik. (1987) via http://www.orfeus-eu.org/fdsnws/station/1/query?

[3] *AlpArray Seismic Network (2015)* via https://erde.geophysik.uni-muenchen.de/fdsnws/dataselect/1/query?

2.2. Event detection

Using the knowledge of rockfall activity at the Hochvogel flank between July 9th and 11th 2016, we examined the seismic signals of all stations during this time period. By analyzing the local seismic amplitude and the corresponding spectrograms at each station, we identified all seismic events with the strongest impact at the closest station in Oberstdorf. Rock falls produce a seismic impact over all frequencies between 5 and 50 Hz (Le Roy et al., 2019); We only included events where there is a clear decrease in seismic intensity with increasing distance of the stations from the Hochvogel (strongest in OBER, then RETA, then DAVA) and significant arrival time differences of up to 20 s (first in OBER, then RETA, then A037A, then DAVA) (Figure 3). We excluded earthquakes based on distinct arrivals of P and S waves, a lower frequency content, and small signal arrival times differences between the stations. Most earthquakes could also be linked to an event in the regional and global earthquake event records. Local anthropogenic noise could be identified by higher frequency contents and missing coincidence of the signals between different stations. Following these criteria, we identified all seismic signals potentially originating from the rock fall series at the Hochvogel. We assured the origination of the seismic events at the Hochvogel due to the fact that all signals decay with increasing distance of the station from the Hochvogel, the overall similar arrival time delay patterns, and their coincidence to personal rock fall activity observations by hikers during the analyzed time period.

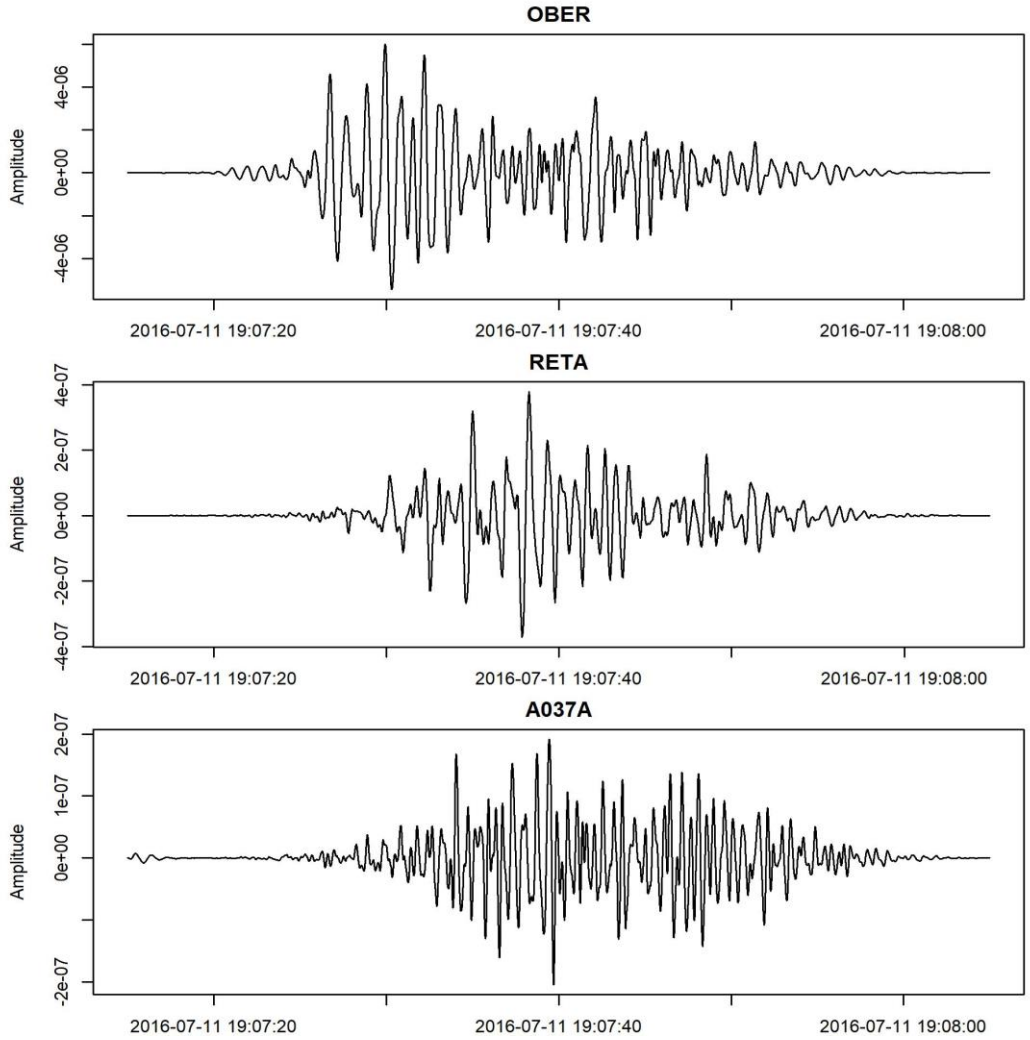

Figure 3. Seismoograms of a rockfall. The intensity of the seismic energy decreases and arrival times increase with increasing distance of the stations from the Hochvogel (strongest in OBER, then RETA, then A037A).

Table 8. Summary of the rockfalls identified between 9th and 11th of July

event	First arrival time at OBER in UTC	status
1	2016-07-09 08:37:45	probably rock fall signal
2	2016-07-09 17:39:27	probably rock fall signal
3	2016-07-11 17:39:36	probably rock fall signal
4	2016-07-11 18:48:13	clearly rock fall signal
5	2016-07-11 19:05:19	clearly rock fall signal
6	2016-07-11 19:07:16	clearly rock fall signal

The latest three seismic events show clear evidence for originating from the Hochvogel rock failure, while the first three events are harder to constrain due to their smaller amplitude. Nevertheless, these also show the same intensity decay and arrival time patterns at the closest stations and can therefore be taken into account. For the parameter estimation, we only used the clear events [4,5,6] in Table 8.

2.3. Parameter estimation

r (distance)

The distance of the seismic stations to the source rock fall at the Hochvogel has been calculated as topography corrected distance using *spatial_migrate( )* from the *eseis* package (Dietze, 2018a, b) The results are listed in Table 9.

Table 9. Distance of each seismic station from the Hochvogel.

ID	distance [m]
OBER	11,783
PART	54,696
ZUGS	41,344
DAVA	43,173
MOTA	53,916
RETA	27,433
A037A	39,224

p (density)

We assume a ground density of the carbonate rock to 2500 ± 100 kg m^{-3} kg m^{-3}.

c (velocity)

The main seismic energy is transported by the surface waves and not the fastest P-waves. We, therefore, estimated the relevant seismic velocity based on the timing of the peak ground velocity and peak envelope value at each station (vertical component) filtered between 1 and 2 Hz (to avoid timely differences and distortion in higher frequencies). The velocity is found by the linear regression of the time difference and the distance difference for each station pair as 1715 ± 99 m s^{-1} (Figure 4).

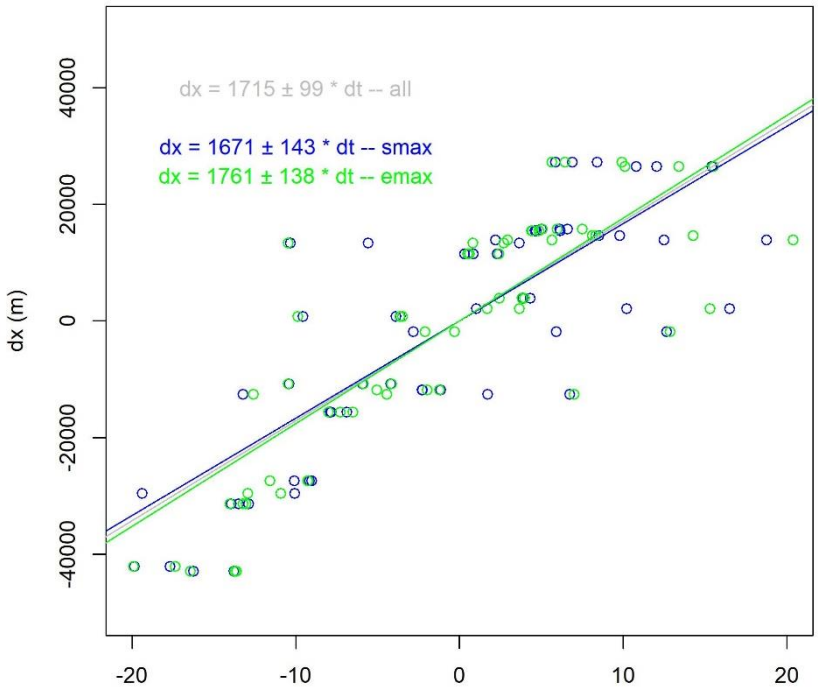

Figure 4. Linear regression for the estimation of the parameter c (velocity)

h (thickness of layer)

The centroid frequency (f_centroid) of the seismic signals is 4.93 ± 0.92 Hz (calculated with *signal_stats()* from eseis). We, therefore, estimated the thickness of the layer through which the surface waves travel as one Rayleigh wavelength with h = c/f_centroid.

t0 and t1

Onset and end times of seismic events have been picked manually from the filtered seismograms.

u_{env} (envelope)

The envelope of the seismic signal has been calculated using the *signal_envelope()* function from the eseis package.

ε (site effect coefficient)

We used the 10 strongest earthquakes of 2016 recorded by all stations (Table 10) to estimate the amplitude correction of each station relative to the OBER station (reference station, ε = 1). ε has been set as the mean ratio

of peak signal envelope relative to OBER in the vertical component (filtered between 2 and 6 Hz containing the most energy around the frequency centroid). The results are listed in Table 11.

Table 10. Earthquakes used for the calculation of the parameter ε (site effect coefficient). Data source: USGS (2022)

Magnitude.	Location	Depth [km]	Origin time (UTC)	Region
7.9	4.505°S 153.522°E	94.5	2016-12-17 10:51:10	Kokopo, Papua New Guinea
7.8	42.737°S 173.054°E	15.1	2016-11-13 11:02:56	Amberley, New Zealand
7.8	0.382°N 79.922°W	20.6	2016-04-16 23:58:36	Muisne, Ecuador
7.8	4.952°S 94.330°E	24.0	2016-03-02 12:49:48	Sumatra, Indonesia
7.7	18.543°N 145.507°E	196.0	2016-07-29 21:18:24	Northern Mariana Islands
7.4	55.285°S 31.877°W	10.0	2016-08-19 07:32:22	South Georgia Island
7.2	22.477°S 173.117°E	16.4	2016-08-12 01:26:36	Loyalty Islands
7.2	56.241°S 26.935°W	78.0	2016-05-28 09:46:59	South Sandwich Islands
7.2	53.978°N 158.546°E	177.0	2016-01-30 03:25:12	Mil'kovo, Russia
7.1	0.046°S 17.826°W	10.0	2016-08-29 04:29:57	Ascension Island

Table 11. Summary of the estimated values for the parameter ε (site effect coefficient) for each seismic station.

ID	ε (mean)	ε (sd)
OBER	1.000000	0.0000000
PART	1.333635	0.4460248
ZUGS	2.870155	1.4927984
DAVA	3.032414	0.5136714
MOTA	3.730635	1.6229273
RETA	5.529136	1.1359063
A037A	3.086086	1.3231271

α (attenuation factor)

The attenuation factor has been estimated following the description of Le Roy et al. (2019) with a correction of the index typo i and j following Kanai et al. (1984) using the 3 rock fall events [4,5,6] and filtered vertical components between 2 and 6 Hz containing the most energy up to the frequency centroid:

$$log_e\left[\frac{a_i\varepsilon_j}{a_j\varepsilon_i}\left(\frac{r_i}{r_j}\right)^n\right] = -\alpha(r_i - r_j) \quad (8)$$

With α being the amplitude of a station pair i and j, n being 0.5 for surface waves and α being the attenuation factor. α has then been determined by a linear regression of the logarithm term and ($r_i - r_j$) (Figure 5).

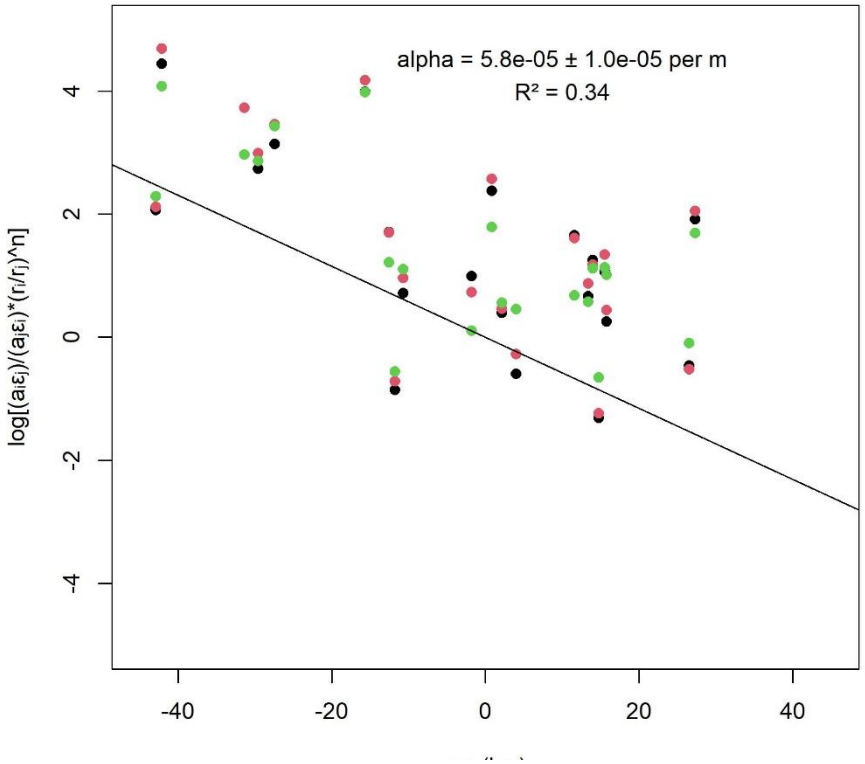

Figure 5. Linear regression for the estimation of the parameter α (attenuation factor)

H (fall height)

The fall height has been estimated by analyzing the 3D point clouds and DEM differences. A simple toppling of the center of gravity towards the slope corresponds to a fall height of 50-60 m while a sliding of the failed block suggests a probable fall height of 75 to 100 m.

2.4. Error estimation

All parameters have been estimated with a range or as mean with standard deviation. To estimate the error of the final volume calculation, we used 1,000 iterations of a Monte Carlo simulation, where p is picked as a random deviate between the min and max values and c, h, α and ε are randomly generated values with the respective mean and standard deviation. This allows us to give a statistical range for the result of each sub-event at each station.

Additionally, we calculated the volume for all stations, although OBER is the closest station and therefore, the results are most reliable here.

2.5. Results

The stations PART and ZUGS had to be excluded due to the bad signal-to-noise ratio of the rock fall signal. The volume estimation for each sub-event is summarized in Figure 6 and Table 12.

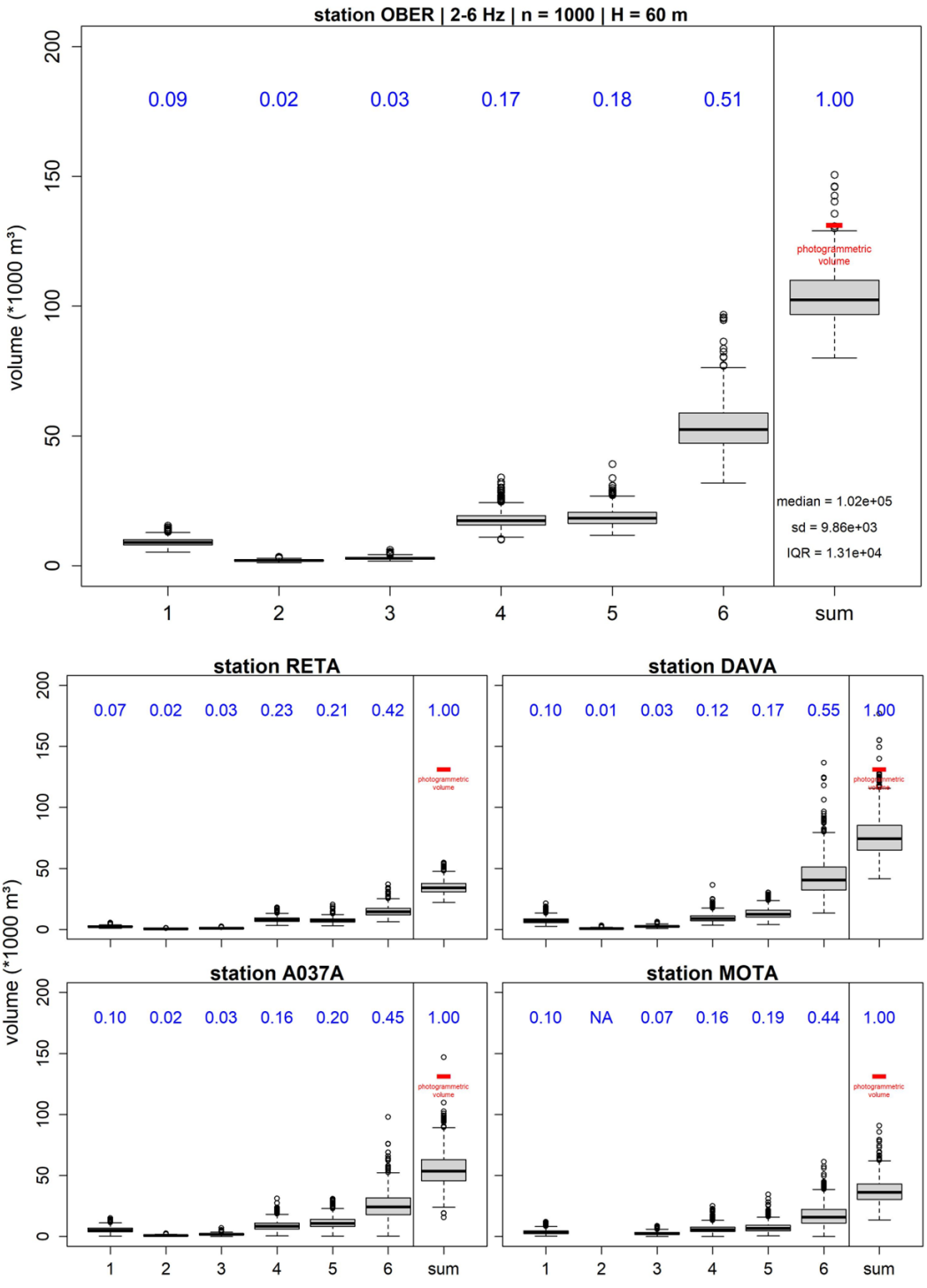

Figure 6. Volume estimation for each sub-event using a Monte-Carlo simulation with 1,000 iterations for each seismic station.

Table 12. Cumulative median total volume for each seismic station for different fall heights.

	OBER		RETA		DAVA		A037A		MOTA		MEAN
fall height [m]	median	sd	median	sd	median	sd	median	sd	median	sd	
50	122,946	11,826	40,922	6,254	89,157	20,050	64,349	16,506	43,433	12,658	**72,161**
60	102,455	9,855	34,101	5,211	74,297	16,709	53,624	13,755	36,194	10,548	**60,134**
75	81,964	7,884	27,281	4,169	59,438	13,367	42,899	11,004	28,955	8,438	**48,107**
100	61,473	5,913	20,461	3,127	44,578	10,025	32,174	8,253	21,716	6,329	**36,081**

For all other stations, the respective sub-event´s percentage of the total volume is very similar (Table 13). The stations further away than OBER underestimate the volume due to stronger signal damping, distortion, and worse coupling compared to the closest station OBER.

Table 13. Percentage of the total volume per seismic station

	OBER	RETA	DAVA	A037A	MOTA	MEAN
sub-event #1	0.09	0.07	0.1	0.1	0.1	0.09
sub-event #2	0.02	0.02	0.01	0.02	0.00	0.01
sub-event #3	0.03	0.03	0.03	0.03	0.07	0.04
sub-event #4	0.17	0.23	0.12	0.16	0.16	0.17
sub-event #5	0.18	0.21	0.17	0.2	0.19	0.19
sub-event #6	0.51	0.42	0.55	0.45	0.44	0.47

References

AlpArray Seismic Network, AlpArray Seismic Network (AASN) temporary component. [Data set] AlpArray Working Group. Other/Seismic Network. https://doi.org/10.12686/alparray/z3_2015, 2015

Dietze, M.: “eseis” - a comprehensive R software toolbox for environmental seismology, GFZ Data Services, 2018a.

Department of Earth and Environmental Sciences, Geophysical Observatory, University of Munchen. BayernNetz [Data set]. International Federation of Digital Seismograph Networks. https://doi.org/10.7914/SN/BW, 2001.

Dietze, M.: The R package eseis – a comprehensive software toolbox for environmental seismology, Earth Surf. Dynam, 1–28, https://doi.org/10.5194/esurf-2017-75, 2018b.

Kanai, K., Yamabe, K., and Habasaki, A.: Study of the attenuation of seismic waves, in: Proceedings of the Eighth World Conference on Earthquake Engineering, 273–280, 1984.

Le Roy, G. L., Helmstetter, A., Amitrano, D., Guyoton, F., and Roux-Mallouf, R. L.: Seismic Analysis of the Detachment and Impact Phases of a Rockfall and Application for Estimating Rockfall Volume and Free-Fall Height, J Geophys Res Earth Surf, 124, 2602–2622, https://doi.org/10.1029/2019jf004999, 2019.

U.S. Geological Survey (2022), Earthquake Catalogue, accessed 2022-12-08 at URL https://earthquake.usgs.gov/earthquakes/map/?extent=-89.74899,-382.5&extent=89.74589,742.5&range=search&timeZone=utc&search=%7B%22name%22:%22Search%20Results%22,%22params%22:%7B%22starttime%22:%222016-07-01%2000:00:00%22,%22endtime%22:%222016-07-31%2023:59:59%22,%22minmagnitude%22:2.5,%22orderby%22:%22time%22%7D%7D

ZAMG - Zentralanstalt für Meterologie und Geodynamik, Austrian Seismic Network [Data set]. International Federation of Digital Seismograph Networks. https://doi.org/10.7914/SN/OE, 1987.